Science

AAAS

Atomic-Scale Visualization of Inertial Dynamics
A. M. Lindenberg, *et al.*
Science **308**, 392 (2005);
DOI: 10.1126/science.1107996

References and Notes

1. N. V. Prokof'ev, P. C. E. Stamp, *Rep. Prog. Phys.* **63**, 669 (2000).
2. R. P. Feynman, F. L. Vernon, *Ann. Phys.* **24**, 118 (1963).
3. W. Wernsdorfer, S. Bhaduri, R. Tiron, D. N. Hendrickson, G. Christou, *Phys. Rev. Lett.* **89**, 197201 (2002).
4. A. Osterloh, L. Amico, G. Falci, R. Fazio, *Nature* **416**, 608 (2002).
5. S. Sachdev, *Phys. World* **12**, 33 (1999).
6. S. Sachdev, *Quantum Phase Transitions* (Cambridge Univ. Press, Cambridge, 1999).
7. P. G. de Gennes, *Solid State Commun.* **1**, 132 (1963).
8. R. J. Elliott, P. Pfeuty, C. Wood, *Phys. Rev. Lett.* **25**, 443 (1970).
9. R. B. Stinchcombe, *J. Phys. C* **6**, 2459 and 2484 (1973).
10. D. Bitko, T. F. Rosenbaum, G. Aeppli, *Phys. Rev. Lett.* **77**, 940 (1997).
11. T. F. Rosenbaum *et al.*, *J. Appl. Phys.* **70**, 5946 (1991).
12. D. Bitko, thesis, University of Chicago (1997).
13. R. Giraud *et al.*, *Phys. Rev. Lett.* **87**, 057203 (2001).
14. J. Brooke, D. Bitko, T. F. Rosenbaum, G. Aeppli, *Science* **284**, 779 (1999).
15. J. Brooke, T. F. Rosenbaum, G. Aeppli, *Nature* **413**, 610 (2001).
16. S. Ghosh, R. Parthasarathy, T. F. Rosenbaum, G. Aeppli, *Science* **296**, 2195 (2002).
17. S. Ghosh *et al.*, *Nature* **425**, 48 (2003).
18. K. Andres, *Phys. Rev. B* **7**, 4295 (1973).
19. R. W. Youngblood, G. Aeppli, J. D. Axe, J. A. Griffin, *Phys. Rev. Lett.* **49**, 1724 (1982).
20. H. M. Rønnow, thesis, Risø National Laboratory, Denmark (2000).
21. M. J. M. Leask *et al.*, *J. Phys. C* **6**, 505 (1994).
22. A. P. Ramirez, J. Jensen, *J. Phys. C* **6**, L215 (1994).
23. J. Magariño, J. Tuchendler, P. Beauvillain, I. Laursen, *Phys. Rev. B* **21**, 18 (1980).
24. G. Mennenga, L. J. de Jongh, W. J. Huiskamp, *J. Magn. Magn. Mater.* **44**, 59 (1984).
25. H. M. Rønnow *et al.*, in preparation.
26. J. Jensen, *Phys. Rev. B* **49**, 11833 (1994).
27. P. B. Chakraborty, P. Henelius, H. Kjønsberg, A. W. Sandvik, S. M. Girvin, *Phys. Rev. B* **70**, 144411 (2004).
28. P. Gegenwart *et al.*, *Phys. Rev. Lett.* **89**, 056402 (2002).
29. P. C. E. Stamp, I. S. Tupitsyn, *Phys. Rev. B* **69**, 014401 (2004).
30. We thank G. McIntyre for his expert assistance during complementary measurements on the D10 diffractometer at the Institut Laue Langevin, Grenoble, France. Work at the University of Chicago was supported by NSF Materials Research Science and Engineering Centers grant DMR-0213745. Work in London was supported by the Wolfson–Royal Society Research Merit Award Program and the Basic Technologies program of the UK Research Councils.

Atomic-Scale Visualization of Inertial Dynamics

A. M. Lindenberg,[1] J. Larsson,[2] K. Sokolowski-Tinten,[3]
K. J. Gaffney,[1] C. Blome,[4] O. Synnergren,[2] J. Sheppard,[5]
C. Caleman,[6] A. G. MacPhee,[7] D. Weinstein,[7] D. P. Lowney,[7]
T. K. Allison,[7] T. Matthews,[7] R. W. Falcone,[7] A. L. Cavalieri,[8]
D. M. Fritz,[8] S. H. Lee,[8] P. H. Bucksbaum,[8] D. A. Reis,[8] J. Rudati,[9]
P. H. Fuoss,[10] C. C. Kao,[11] D. P. Siddons,[11] R. Pahl,[12]
J. Als-Nielsen,[13] S. Duesterer,[4] R. Ischebeck,[4] H. Schlarb,[4]
H. Schulte-Schrepping,[4] Th. Tschentscher,[4] J. Schneider,[4]
D. von der Linde,[14] O. Hignette,[15] F. Sette,[15] H. N. Chapman,[16]
R. W. Lee,[16] T. N. Hansen,[2] S. Techert,[17] J. S. Wark,[5] M. Bergh,[6]
G. Huldt,[6] D. van der Spoel,[6] N. Timneanu,[6] J. Hajdu,[6]
R. A. Akre,[18] E. Bong,[18] P. Krejcik,[18] J. Arthur,[1] S. Brennan,[1]
K. Luening,[1] J. B. Hastings[1]

The motion of atoms on interatomic potential energy surfaces is fundamental to the dynamics of liquids and solids. An accelerator-based source of femtosecond x-ray pulses allowed us to follow directly atomic displacements on an optically modified energy landscape, leading eventually to the transition from crystalline solid to disordered liquid. We show that, to first order in time, the dynamics are inertial, and we place constraints on the shape and curvature of the transition-state potential energy surface. Our measurements point toward analogies between this nonequilibrium phase transition and the short-time dynamics intrinsic to equilibrium liquids.

In a crystal at room temperature, vibrational excitations, or phonons, only slightly perturb the crystalline order. In contrast, liquids explore a wide range of configurations set by the topology of a complex and time-dependent potential energy surface (*1*, *2*). By using light to trigger changes in this energy landscape, well-defined initial and final states can be generated to which a full range of time-resolved techniques may be applied. In particular, light-induced structural transitions between the crystalline and liquid states of matter may act as simple models for dynamics intrinsic to the liquid state or to transition states in general (*3*).

In this context, a new class of nonthermal processes governing the ultrafast solid-liquid melting transition has recently emerged, supported by time-resolved optical (*4–7*) and x-ray (*8–10*) experiments and with technological applications ranging from micromachining to eye surgery (*11*). Intense femtosecond excitation of semiconductor materials results in the excitation of a dense electron-hole plasma, with accompanying dramatic changes in the interatomic potential (*12–14*). At sufficiently high levels of excitation, it is thought that this process leads to disordering of the crystalline lattice on time scales faster than the time scale for thermal equilibration [often known as the electron-phonon coupling time, on the order of a few picoseconds (*15*)]. In a pioneering study, Rousse *et al.* (*9*) determined that the structure of indium antimonide (InSb) changes on sub-picosecond time scales, but the mechanism by which this occurs and the

microscopic pathways the atoms follow have remained elusive, in part because of uncertainties in the pulse duration of laser-plasma sources and signal-to-noise limitations.

Research and development efforts leading toward the Linac Coherent Light Source (LCLS) free-electron laser have facilitated the construction of a new accelerator-based x-ray source, the Sub-Picosecond Pulse Source (SPPS), which uses the same linac-based acceleration and electron bunch compression schemes to be used at future free-electron lasers (*16*, *17*). In order to produce femtosecond x-ray bursts, electron bunches at the Stanford Linear Accelerator Center (SLAC) are chirped and then sent through a series of energy-dispersive magnetic chicanes to create 80-fs electron pulses. These pulses are then transported through an undulator to create sub-100-femtosecond x-ray pulses (*18*). In order to overcome the intrinsic jitter between x-rays and a Ti:sapphire-based femtosecond laser

[1]Stanford Synchrotron Radiation Laboratory/Stanford Linear Accelerator Center (SLAC), Menlo Park, CA 94025, USA. [2]Department of Physics, Lund Institute of Technology, Post Office Box 118, S-22100, Lund, Sweden. [3]Institut für Optik und Quantenelektronik, Friedrich-Schiller Universität Jena, Max-Wien-Platz 1, 07743 Jena, Germany. [4]Deutsches Elektronen-Synchrotron DESY, Notkestrasse 85, 22607 Hamburg, Germany. [5]Department of Physics, Clarendon Laboratory, Parks Road, University of Oxford, Oxford OX1 3PU, UK. [6]Department of Cell and Molecular Biology, Biomedical Centre, Uppsala University, SE-75124 Uppsala, Sweden. [7]Department of Physics, University of California, Berkeley, CA 94720, USA. [8]FOCUS (Frontiers in Optical Coherent and Ultrafast Science) Center, Department of Physics and Applied Physics Program, University of Michigan, Ann Arbor, MI 48109, USA. [9]Advanced Photon Source, [10]Materials Science Division, Argonne National Laboratory, Argonne, IL 60439, USA. [11]National Synchrotron Light Source, Brookhaven National Laboratory, Upton, NY 11973, USA. [12]Consortium for Advanced Radiation Sources, University of Chicago, Chicago, IL 60637, USA. [13]Niels Bohr Institute, Copenhagen University, 2100 Copenhagen Ø, Denmark. [14]Institut für Experimentelle Physik, Universität Duisburg-Essen, D-45117 Essen, Germany. [15]European Synchrotron Radiation Facility, 38043 Grenoble Cedex 9, France. [16]Physics Department, Lawrence Livermore National Laboratory, Livermore, CA 94550, USA. [17]Max Plank Institute for Biophysical Chemistry, Am Faßberg 11, 37077 Göttingen, Germany. [18]SLAC, Menlo Park, CA 94025, USA.

system, pump-probe measurements using an InSb sample were conducted in a cross-beam geometry (19, 20) with the optical pump pulse incident at an angle with respect to the x-ray probe pulse. In this way, a temporal sweep is created along the crystal surface that transforms temporal information into spatial information as a result of the difference in propagation times across the sample surface. By imaging the diffracted x-ray spot with a charge-coupled device (CCD) camera, we obtained the complete time history around $t = 0$ in a single shot.

Typical single-shot images are shown in Fig. 1. The top image shows x-rays diffracted from the unperturbed sample. The bottom image is obtained when the pump and probe pulses overlap in space and time on the sample. The sharp edge in the bottom image indicates time zero. To the left of this edge, x-rays scatter from the unperturbed sample before the optical excitation pulse arrives. To the right, x-rays probe the optically induced liquid state, resulting in a strong decrease in the diffracted intensity. Our temporal resolution is set by the pulse duration of the x-ray probe and the accuracy with which we can image the surface topography; we estimated this to be ≤130 fs for the (111) reflection and ≤80 fs for the (220) reflection by imaging the sharp edge of a razor blade placed on the sample surface.

The measured time-dependent intensity values, $I(Q,t)$ (where Q is the reciprocal lattice vector for the reflection probed), for both the (111) and (220) reflections were averaged over 10 single-shot images (Fig. 2) (21). The x-ray incidence angle was kept constant at 0.4° for both reflections by rotating an asymmetrically

cut crystal about its surface normal (the same crystal is used for both reflections). In this way, the x-ray probe depth was fixed at 50 nm (comparable to the laser excitation depth), and the laser spot size was unchanged when switching between different x-ray reflections. Thus, the experiments probed the dynamical behavior for the two reflections under identical conditions. Figure 2 shows (111) and (220) data fit to both exponential and Gaussian decays.

We observe first that, for times after excitation, the diffracted intensity is nonexponential and well-fit by a Gaussian with peak centered at the excitation time. Moreover, the (220) reflection decays with a time constant qualitatively faster than that for the (111). The times for the intensity to fall from 90% to 10% of its initial value for the (111) and (220) reflections are 430 and 280 fs, respectively, with ratio $\tau_{111}/\tau_{220} = 1.5 \pm 0.2$. This value is equal (within experimental error) to the ratio of the magnitude of the reciprocal lattice vectors for the two reflections ($\sqrt{8/3}$).

This inverse Q-dependent scaling and Gaussian time dependence strongly implies statistical atomic motion and suggests that the data can be described with use of a time-dependent Debye-Waller (DW) model, which relates the time-dependent decrease in scattered intensity to a time-dependent root mean square (RMS) displacement:

$$I(Q,t) = e^{-2W} = e^{-Q^2 \langle u^2(t) \rangle / 3} \quad (1)$$

Here, W is the standard DW factor and $\langle u^2(t) \rangle$ is the time-dependent mean-square displacement of the photoexcited atoms averaged spatially over the sample. This

model makes physical sense if the disordering process can be described as an effective amplification of the RMS displacements characteristic of a room temperature thermal distribution, preserving $\langle u \rangle = 0$. The time-averaged assumption that is usually made in the derivation of the DW factor may then be replaced by a spatial average over all excited atoms (22). A time-dependent increase in the RMS displacement is indeed what one would expect given the strong optically induced modification of the potential surface. After an impulsive softening of the interatomic potential and for short times afterward (to first order in time), the atoms continue to move with velocities set by initial conditions, i.e., inertially, following Newton's Third Law. To first order in time, with $\langle u^2(t) \rangle^{1/2} = v_{rms}t$, the time-resolved diffracted intensity $I(Q,t)$ is then expected to decay as $I(t) \sim e^{-Q^2 v_{rms}^2 t^2 / 3}$, i.e., Gaussian in both Q and t with a time constant that varies inversely with Q, exactly as observed.

The validity of this model was checked in three different ways: (i) comparison of the extracted RMS displacements for the (111) and (220) reflections, (ii) comparison of the
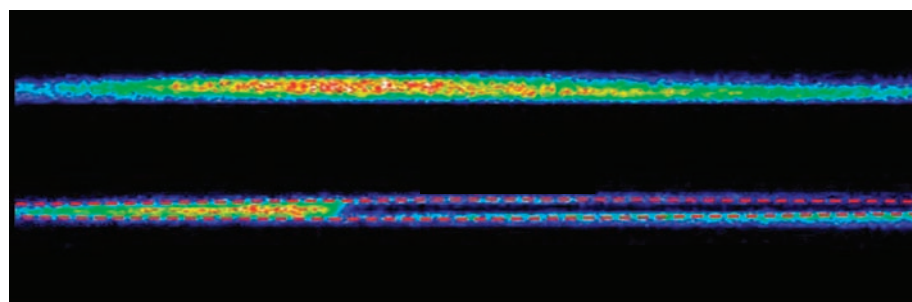

Fig. 1. (Top) A single-shot image of scattered x-rays from unperturbed sample above a single-shot image of perturbed sample. Dashed curves show region excited by laser pulse. **(Bottom)** Experimental setup showing cross-beam topography technique. By crossing the pump and probe beams on the sample and imaging the diffracted x-rays, we mapped temporal information into spatial information, enabling collection of the complete time history around time zero in a single shot. Time runs from left to right. The time window shown is ~8 ps.
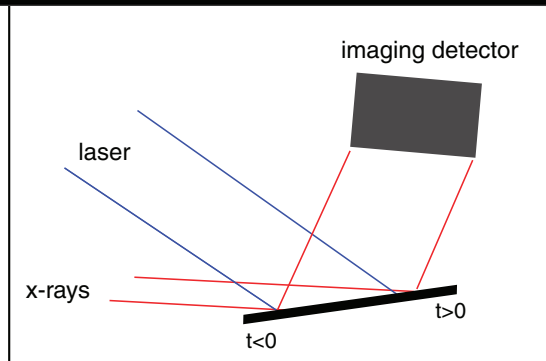
Fig. 2. Time-dependent diffracted intensity for (111) **(top)** and (220) **(bottom)** reflections, measured under identical excitation conditions. Red curves are Gaussian fits to the data, corresponding to 10 to 90% fall times of 430 fs and 280 fs. Blue curve is an exponential fit. (Inset) Fluence dependence of 10 to 90 time constants for (111) data. Error bars reflect the standard deviation of the mean, determined from the scatter in the individual measurements.

measured velocity of the atoms to room temperature excitations, and (iii) fluence dependence of the time-constants of the decay of the diffracted intensity. Extracted RMS displacements for the (111) and the (220) reflections are shown in Fig. 3, obtained by using Eq. 1 to invert the raw $I(Q,t)$ data. For short times, the two curves overlap well, indicating an initial isotropic-disordering process, independent of reciprocal lattice vector. (At long times, different final displacements derived from the two reflections may imply an anisotropy in the disordering process and/or a breakdown in the DW model; however, uncertainty in the effective laser penetration depth makes this conclusion uncertain.)

Second, for short times, we observe that the RMS displacements are linear in time, with a slope (corresponding to a velocity) of 2.3 Å/ps. This value is in good agreement with room temperature RMS velocities in InSb [$(3k_bT/M)^{1/2} = 2.5$ Å/ps, where M is the average mass of InSb and $T = 300$ K (23)]. Lastly, the Fig. 2 inset shows the fluence dependence of the time constants for the (111) reflection. There is little variation with fluence (a similar result is obtained for the 220 reflection). Thus, as might be expected for short times, it is difficult to tell the difference between a flat potential (corresponding to a free particle) and a motion driven by a softened phonon with an imaginary frequency (corresponding to a saddle point on the potential energy surface). From our data, we can place both an upper and lower bound on the extent of the softening of the potential surface. At very large softenings, we expect to observe acceleration of the atoms as they fall down the potential energy surface. Because we observe that the
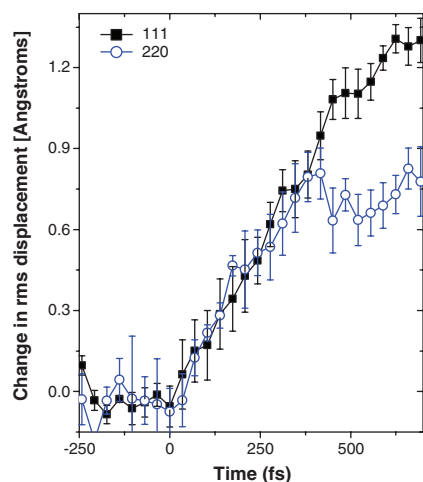
dynamics remain inertial for at least 250 fs, it can be shown (neglecting anharmonicities in the potential) that this requires a negative curvature ≤1 eV/Å². Similarly, that we observe displacements on the order of 1 Å from the equilibrium position implies a maximum positive curvature (corresponding to a real frequency) of ∼0.1 eV/Å², which represents a dramatic change in the interatomic potential. Figure 4 illustrates the changes in the interatomic potential and atomic-scale displacements calculated on the basis of this model. The implication is then of a transition state in which the interatomic potential is softened enough that the atoms initially move freely with large amplitude along an effectively barrierless potential energy surface with initial conditions set by room-temperature thermodynamic velocities. This simple model fits all of our data at short times with no adjustable parameters.

The dynamics we observe during the ultrafast transition of a crystalline solid into a liquid show similarity with the intrinsic short time dynamics observed in equilibrium liquids from frequency-domain inelastic neutron scattering and molecular dynamics simulations (24, 25). Indeed, one may show (26) that the RMS displacement of an atom in the liquid state obeys

$$u^2(t) = \frac{3k_BT}{M}t^2 - \frac{k_bT}{4M}\Omega^2 t^4 \qquad (2)$$

where Ω is a collision frequency. To first order in time, the dynamics are inertial, with atoms moving at their thermal velocities along

a potential landscape characteristic of the instantaneous atomic positions. Our results thus indicate that, at short times, the ultrafast solid-liquid transition may be viewed as representative of the short time-scale structural rearrangements intrinsic to the liquid state. At longer times, atoms begin to collide and a transition to a diffusive regime occurs. Although we resolve an inertially driven divergence of the mean square displacements [typically associated with solid-liquid transitions (27) but here observed before any heat is transferred to the lattice], we do not observe clear evidence of diffusive dynamics. This would manifest itself in the tail of the decay in the diffracted intensity as an exponential rather than a Gaussian time response (with $u \sim t^{1/2}$ one obtains this result). Thus, during the first few hundred femtoseconds, although the lattice displacements correspond to a large fraction of the interatomic distances and the strong covalent bonds characteristic of the crystalline state are broken or strongly modified, the average displacement $\langle u(t) \rangle$ from the equilibrium lattice sites is still zero, reflective of the initial crystalline state. In this respect, for the first few hundred femtoseconds, the state of the system is intermediate between that of a solid and that of a liquid.

References and Notes
1. F. H. Stillinger, T. A. Weber, *Phys. Rev. A.* **25**, 978 (1982).
2. R. Stratt, *Accts. Chem. Res.* **28**, 201 (1995).
3. B. J. Siwick et al., *Science* **302**, 1382 (2003).
4. C. Shank, R. Yen, C. Hirlimann, *Phys. Rev. Lett.* **51**, 900 (1983).
5. I. Shumay, U. Hofer, *Phys. Rev. B* **53**, 15878 (1996).
6. K. Sokolowski-Tinten, J. Bialkowski, D. von der Linde, *Phys. Rev. B* **51**, 14186 (1995).
7. S. Sundaram, E. Mazur, *Nat. Mater.* **1**, 217 (2002).
8. C. Siders et al., *Science* **286**, 1340 (1999).
9. A. Rousse et al., *Nature* **410**, 65 (2001).
10. K. Sokolowski-Tinten et al., *Phys. Rev. Lett.* **87**, 225701 (2001).
11. X. Lui, D. Du, G. Mourou, *IEEE J. Quantum Electron.* **33**, 1706 (1997).
12. P. Stampfli, K. Bennemann, *Phys. Rev. B* **49**, 7299 (1994).
13. T. Dumitrica, A. Burzo, Y. Dou, R. Allen, *Phys. Status Solidi B* **241**, 2331 (2004).
14. H. O. Jeschke et al., *Appl. Surf. Sci.* **197**, 839 (2002).
15. A. H. Chin et al., *Phys. Rev. Lett.* **83**, 336 (1999).
16. P. Krejcik et al., in *Proceedings of the 2003 Particle Accelerator Conference*, IEEE, Portland, OR, 12 to 16 May 2003, J. Chew, P. Lucas, S. Webber, Eds. (IEEE, Piscataway, NJ, 2003), p. 423.
17. R. Service, *Science* **298**, 1356 (2002).
18. Measurements of electron bunch length and energy spread as they evolve through the SLAC linac are in good agreement with the particle tracking codes used to predict 80-fs bunches. Measurements by interferometric autocorrelation of the coherent transition radiation from the electron bunches are also consistent with 80-fs electron bunches. These independent measurements provide strong evidence that our estimates of the x-ray pulse duration as well as the pulse shape at optimal compression are accurate.
19. O. Synnergren et al., *Appl. Phys. Lett.* **80**, 3727 (2002).
20. R. Neutze, J. Hajdu, *Proc. Natl. Acad. Sci. U.S.A.* **94**, 5651 (1997).
21. The measured time constants are in good agreement with the average of the time constants extracted from each image. By comparing our measurements with independent measurements of the electron-bunch arrival time, we estimate that the relative timing of laser and x-rays from shot to shot can be determined to better than 60 fs by spatially recording the midpoint of the sudden drop in diffracted intensity (28).
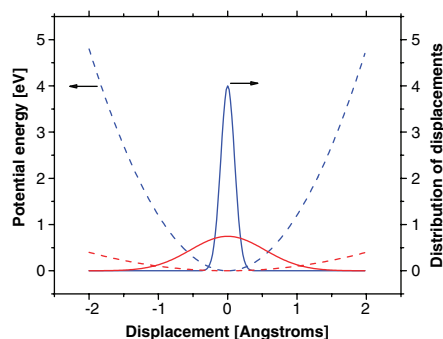
Fig. 3. The change in the RMS displacement $\sqrt{\delta u^2(t)}$ extracted from the time-dependent diffracted intensity with use of the DW model. For short times, the measured displacements agree well for both x-ray reflections, validating the model. The slope corresponds to a velocity in good agreement with the room-temperature RMS velocity in InSb.

Fig. 4. One-dimensional illustration of changes in the interatomic potential (dashed) and distribution of atomic displacements (solid) from the equilibrium state. Blue curves refer to the unperturbed state, and red curves refer to $t = 200$ fs after excitation. At equilibrium and at room temperature in InSb, RMS displacements are ∼0.1 Å (29). The interatomic potential for this case is calculated by using equipartition and an assumption of one-dimensional simple harmonic behavior. At $t = 200$ fs, we measure RMS displacements ∼ 0.5 Å corresponding to a substantial fraction of the interatomic spacing. The softened potential shown (dashed red) corresponds to the minimum softening required (0.1 eV/Å²) to be consistent with our experimental results.

22. P. Liu, P. Okamoto, N. Zaluzec, M. Meshii, *Phys. Rev. B* **60**, 800 (1999).
23. G. L. Squires, *Introduction to the Theory of Thermal Neutron Scattering* (Cambridge Univ. Press, Cambridge, 1978).
24. B. Dasannacharya, K. Rao, *Phys. Rev.* **137**, A417 (1965).
25. A. Paskin, A. Rahman, *Phys. Rev. Lett.* **16**, 300 (1966).
26. U. Balucani, M. Zoppi, *Dynamics of the Liquid State* (Clarendon Press, Oxford, 1994).
27. F. Lindemann, *Phys. Z.* **11**, 609 (1910).
28. A. Cavalieri *et al.*, *Phys. Res. Lett.*, in press.
29. J. F. Vetelino, S. P. Gaur, S. S. Mitra, *Phys. Rev. B* **5**, 2360 (1972).
30. Portions of this research were supported by the U.S.

A Convergent Enantioselective Route to Structurally Diverse 6-Deoxytetracycline Antibiotics

Mark G. Charest, Christian D. Lerner, Jason D. Brubaker, Dionicio R. Siegel, Andrew G. Myers*

Complex antibiotics based on natural products are almost invariably prepared by semisynthesis, or chemical transformation of the isolated natural products. This approach greatly limits the range of accessible structures that might be studied as new antibiotic candidates. Here we report a short and enantioselective synthetic route to a diverse range of 6-deoxytetracycline antibiotics. The common feature of this class is a scaffold of four linearly fused rings, labeled A through D. We targeted not a single compound but a group of structures with the D ring as a site of structural variability. A late-stage, diastereoselective C-ring construction was used to couple structurally varied D-ring precursors with an AB precursor containing much of the essential functionality for binding to the bacterial ribosome. Five derivatives were synthesized from benzoic acid in yields ranging from 5 to 7% over 14 to 15 steps, and a sixth, (–)-doxycycline, was synthesized in 8.3% yield over 18 steps.

The limitations of chemical synthesis frequently present a substantial obstacle to the development and discovery of new antibiotics and of pharmaceutical agents in general. The problem is nowhere more evident than among the structurally complex natural products tetracycline (**1**) and erythromycin. Both agents have proven highly effective in treating a wide range of bacterial infections, but decades of clinical use have led to the emergence of widespread bacterial resistance and, as a result, a need for the development of new antibiotics (*1–3*). The approach to the synthesis of varied structures in these classes has changed little in more than 50 years of research and is largely restricted to a process of semisynthesis, whereby the natural product is isolated and then modified, although approaches based on modified biosynthetic pathways are under development (*4–6*).

The tetracycline class of molecules is characterized by a carbon skeleton composed of four linearly fused six-membered carbon rings, conventionally labeled A through D

Department of Chemistry and Chemical Biology, Harvard University, Cambridge, MA 02138, USA.

*To whom correspondence should be addressed. E-mail: myers@chemistry.harvard.edu

(Fig. 1A). Among the derivatives accessed by semisynthesis, those with the hydroxyl group removed from carbon 6 of the C ring have shown particular clinical promise. These 6-deoxytetracyclines are considerably more resistant to degradation than their 6-hydroxy counterparts, and they show equal or greater potencies in antibacterial assays (*7, 8*). The clinical efficacy of 6-deoxytetracyclines such as doxycycline (**2**) and minocycline (**3**) argues for a broad evaluation of 6-deoxytetracyclines. Unfortunately, the elaboration of natural tetracyclines is greatly limiting in terms of scope, and a general synthetic route to diverse tetracyclines has been elusive.

Here we report a short and efficient route for the synthesis of enantiomerically pure members of the 6-deoxytetracyclines from benzoic acid. The route we describe allows for the synthesis of 6-deoxytetracyclines (both with and without a hydroxyl group at C5) by a late-stage coupling reaction of the AB precursors **4** or **5** (Figs. 1B and 2) and provides access to a wide range of 6-deoxytetracyclines with modified D rings, as illustrated by the preparation of (–)-doxycycline (**2**), (–)-6-deoxytetracycline (**6**), the D-ring heterocyclic derivatives **7** and **8**, 10-deoxysancycline (**9**), and the pentacycline derivative **10** (see Fig. 3 for structures). The advantage of the late-stage
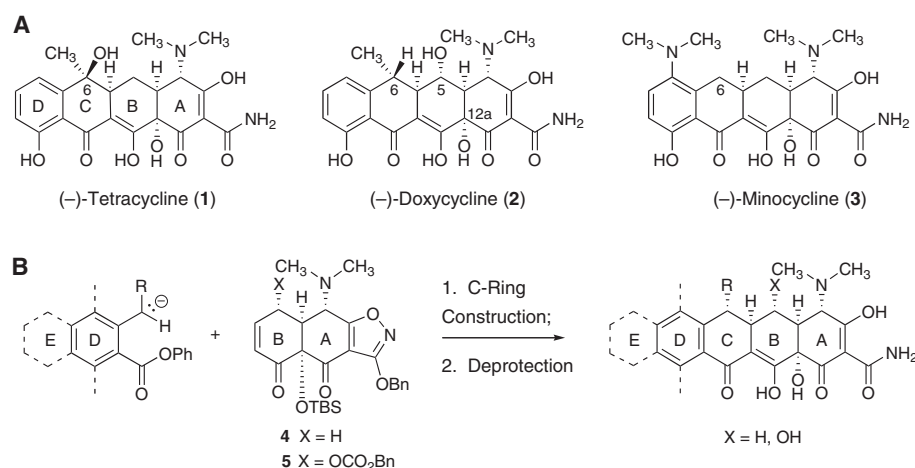
Fig. 1. (**A**) Chemical structures of tetracycline antibiotics. (–)-Tetracycline (**1**) was first produced semisynthetically, by hydrogenolysis of the fermentation product aureomycin (7-chlorotetracycline), but later was discovered to be a natural product and is now produced by fermentation (*8*). (–)-Doxycycline (**2**) and minocycline (**3**) are clinically important non-natural antibiotics and are both manufactured by multistep chemical transformations of fermentation products (semisynthesis) (*8*). (**B**) A generalized Michael-Dieckmann reaction sequence that forms the C ring of tetracyclines from the coupling of structurally varied carbanionic D-ring precursors with either of the AB precursors **4** or **5**.

ERRATUM

Post date 24 June 2005

Reports: "Atomic-scale visualization of inertial dynamics" by A. M. Lindenberg *et al.* (15 Apr. 2005, p. 392). Reference 28 was incorrect. It should be A. L. Cavalieri *et al.*, *Phys. Rev. Lett.* **94**, 114801 (2005).